Photonic High-Power Continuous Wave THz-Wave Generation by Using Flip-Chip Packaged Uni-Traveling Carrier Photodiodes and a Femtosecond Optical Pulse Generator

Jhih-Min Wun, Hao-Yun Liu, Yu-Lun Zeng, Shang-Da Yang, Ci-Ling Pan, *Fellow, IEEE*, Chen-Bin Huang, and Jin-Wei Shi, *Senior Member, IEEE*

***Abstract*—The design, analysis, and demonstration of flip-chip bonding packaged uni-traveling-carrier photodiodes (UTC-PDs) with THz (dc to 315 GHz) 3-dB bandwidth and high-power performance are reported. The high-frequency roll-off (up to 0.4 THz) of the flip-chip bonding structure and device heating under high power operation are both minimized through properly downscaling the area of the bonding pad and minimizing the solder distance to the active area of the miniaturized UTC-PD. In order to suppress the serious space-charge screening effect in miniaturized UTC-PDs under high-current density ($\sim$180 kA/cm^2) operation, an n-type charge layer is inserted into the collector. The detailed dynamic measurement results of these packaged PD modules indicate that non-equilibrium electron transport plays an important role in determining the maximum speed and THz output power. In addition, a femtosecond (fs) optical pulse train generator with a $\sim$300 fs pulse-width output and repetition rate up to $\sim$0.3 THz is also developed to further boost the photo-generated THz-power. Compared with using an optical signal with a sinusoidal envelope for PD excitation, the short-pulse approach can offer a 3-dB enhancement in output power under the same output photocurrent and operating frequency (around 0.3 THz). By utilizing such an fs light source and our PD module, a continuous wave output power as high as 1 mW at an operating frequency of $\sim$0.3 THz is successfully demonstrated.**

***Index Terms*—Photodiodes, packaging, pulse generation.**

I. Introduction

COMMANDING the full electromagnetic (EM) spectrum (near 1 MHz to around 0.3 THz), which includes generation, modulation, wireless transmission, and detection, plays an important role in modern electronic warfare [1], THz bandwidth measurement instruments (network analyzer) [2], and the next-generation of wireless communication at the millimeter-wave or THz wave bands [3]. However, there are many challenges to building a THz system which can cover and process such a wide bandwidth (from 0 Hz–0.3 THz), such as the limited fractional bandwidth of the impedance matching circuit and the very high propagation loss (and dispersion) in either a millimeter-wave (MMW) coaxial cable or metallic waveguide near the THz regime. These difficulties can result in problems with system level interconnection and integration. The photonic approach is one possible solution to overcome the aforementioned problems. The use of an optical fiber as the transmission line in the photonic-assisted THz system can greatly reduce the huge loss and dispersion that occurs in metallic THz waveguides and coaxial cables [1]. A photonic sub-THz wireless communication system [3]–[6] with a 100 Gb/s transmission data rate, photonic MMW measurement instrument (network analyzer) with a broad bandwidth (dc to 200 GHz) [7], and a photonic W-band MMW radar system with ultra-high (3 mm) range resolution have been demonstrated [8]. In these systems, ultra-fast photodiodes (PDs) serve as the key component, which usually determines the maximum allowable operating frequency and dynamic range (output power). Uni-traveling carrier photodiodes (UTC-PDs) [9], [10], which have only fast electrons as active carriers, are one of the most successful high-power and high-speed PD structures for these applications. An extremely wide 3-dB optical-to-electrical (O-E) bandwidth at the THz regime ($\sim$0.31 THz) but with a small output power, has been demonstrated, mainly due to the low load resistance (12.5 Ω) [11]. In addition, the responsivity of ultra-fast UTC-PDs designed for vertical-illumination and with miniaturized size of active area (16 μm^2) is usually small, typically in the range of $\sim$0.03 A/W [12]. The development of a packaging structure for a sub-THz PD with a wide-bandwidth, high output power, and reasonable responsivity performance is thus very important for practical use. Recently, a high output power ($\sim$1.2 mW) has been demonstrated at 300 GHz with a limited fractional bandwidth by using a well-packaged photomixer module, composed of a pair of UTC-PDs with T-junction power combining structures on a quartz substrate [13]. The optical source for THz power generation employed is a simple two-laser heterodyne-beating system. However, the frequency response cannot extend to the dc because of the characteristics of the waveguide based approach and the resonant type impedance-matching circuit (short-stub).

Manuscript received June 29, 2015; revised October 22, 2015; accepted November 22, 2015. Date of publication November 24, 2015; date of current version February 10, 2016. This work was supported by Agilent Technologies Research Grant #3230 and the National Science Council of Taiwan under Grant NSC 101-2221-E-007-103-MY3 and the Ministry of Science and Technology of Taiwan under Grant MOST 103-2112-M-007-017-MY3.

J.-M. Wun, Y.-L. Zeng, and J.-W. Shi are with the Department of Electrical Engineering, National Central University, Taoyuan 320, Taiwan (e-mail: p3984011@hotmail.com; winccc0612@gmail.com; jwshi@ee.ncu.edu.tw).

H.-Y. Liu, S.-D. Yang, and C.-B. Huang are with the Institute of Photonics Technologies, National Tsing-Hua University, Hsinchu 300, Taiwan (e-mail: haoyunliu1118@gmail.com; sdyang@ee.nthu.edu.tw; robin@ee.nthu.edu.tw).

C.-L. Pan is with the Department of Physics, National Tsing-Hua University, Hsinchu 300, Taiwan (e-mail: clpan@phys.nthu.edu.tw).

Color versions of one or more of the figures in this paper are available online at http://ieeexplore.ieee.org.

Digital Object Identifier 10.1109/JLT.2015.2503778

In order to realize PD with a wide 3-dB O-E bandwidth covering from dc to hundreds of GHz, a miniaturized size of active area is typically required. However, this could lead to difficulty in optical coupling, exhibiting small responsivity, ease of device-heating, and eventually thermal failure under high-power operation [14]–[16]. One possible solution to mitigate the above-mentioned problems is the flip-chip bonding of PDs onto a co-planar waveguide (CPW) fabricated on a ceramic substrate (for example, aluminum nitride (AlN)) [14]–[17]. The high thermal conductivity of a ceramic substrate would provide a heat sink and improve its saturation power [14]. Furthermore, the back-side illumination scheme as a result of flip-chip bonding could eliminate the injected light from being blocked by the contact metals on the device front-side [12]. In addition, the back-side optical illumination also allows a double pass of injected light through absorption-layer due to the nearly total reflection on the top p-contact metal. Together, these benefits would lead to an improvement in responsivity performance. The flip-chip bonding PD modules with a 3-dB bandwidth of hundreds of GHz (starting from dc), reasonable responsivity ($\sim$0.1 A/W), and high saturation current (around 15 mA) have been demonstrated [14]–[16].

In addition to device-heating, the other major issue limiting the saturation current of a PD is space-charge screening (SCS) effect [18]. For the case of UTC-PD, the SCS effect usually occurs at the junction of absorption and collector layers [9], [18]. SCS slows down the electron drift process in the collector layer, resulting in speed degradation, and limit the maximum output power. By using n-type doping (charge-compensated doping) in the collector layer, the SCS effect inside UTC-PD can be minimized and excellent performance in saturation current (power) has been demonstrated [19].

In this paper, we demonstrate a UTC-PD with novel design for the collector layer (N-UTC-PD) and advanced flip-chip bonding structure enabling high-power THz operation with excellent performance. By inserting an n-type charge layer of proper thickness and doping density into the collector layer of the UTC-PD, the SCS effect is effectively suppressed without the need for an increased reverse bias voltage. Operation at a lower reverse bias voltage prevents degradation in speed and power performance of ultra-fast PDs [10], [16] due to device-heating and inter-valley scattering effect of electron in the collector layer [9], [11], [15]. Similar working principles have been implemented in UTC-PDs with non-uniform collector doping that operate at a lower frequency regime ($\sim$20 GHz) [20]. By optimizing the flip-chip bonding structure to ensure reliable packaging and high-speed performance, we are able to obtain a wide 3-dB bandwidth ($\sim$315 GHz) with a miniaturized active device size ($\sim$3 μm diameter).

Furthermore, in order to enhance the maximum output power in the THz regime ($\sim$300 GHz) and avoid thermal failure under high-power operation, a femto-second optical short pulse train with a repetition rate as high as $\sim$0.3 THz has been used to excite our device [21]–[24]. It can attain a very-high continuous wave (CW) output power of 1.04 mW with a 13 mA saturation current at 280 GHz operation with a dc responsivity at around 0.1 A/W. Compared with previous work [24], we discuss more detailed flip-chip bonding structures optimized for different band (D- and J-band) operations. Furthermore, detailed dynamic analysis of the packaged chips has been performed under different operation modes (CW and pulse), bias voltages, and output photocurrents. These measurement results clearly indicate that non-equilibrium electron transport plays an important role in determining the maximum speed and power of our demonstrated N-UTC-PD structure.

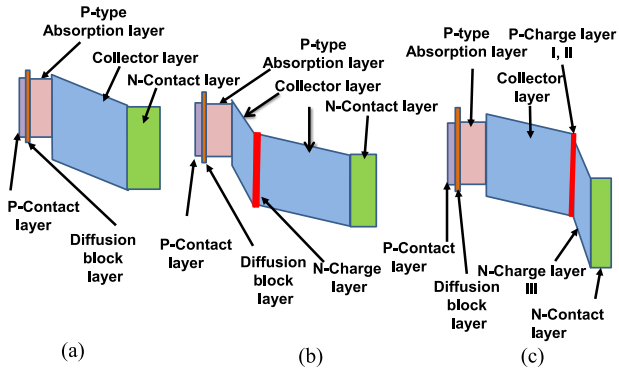

Fig. 1. Conceptual band diagrams of simulated devices: (a) Device A: UTC-PD, (b) Device B: N-UTC-PD, and (c) Device C: NBUTC-PD.

TABLE I
EPI-LAYER STRUCTURE OF DEVICE A: UTC-PD

	A. UTC-PD			
	Material	Thickness (Å)	Doping Level (/cm3)	Type
Graded P-Contact layer	$In_{0.8}Ga_{0.2}As$	100	5.0E+19	p^{++}
P-Contact layer	$In_{0.53}Ga_{0.47}As$	200	2.0E+18	p^{+}
Diffusion Block layer	$In_{0.52}A_{10.29}Ga_{0.19}As$	200	2.0E+18	p^{+}
Absorption layer	$In_{0.53}Ga_{0.47}As$	1500	5E+19 (top) to 5E+17 (bottom)	p^{+}
Collector layer	InP	1600	2.0E+16	N
N Contact layer	InP	7000	5.0E+19	N^{++}
Semi-Insulating InP Substrate	InP			

II. DEVICE STRUCTURE AND DESIGN

In order to understand the advantages of the proposed N-UTC-PD structure for THz applications, we simulate and compare different designs of UTC-PD based device structures. Fig. 1 shows the conceptual band diagram of three kinds of device structure. The simulation is conducted through the use of commercial software (ISE TCAD).[1] Device A is the typical UTC-PD, B is the newly demonstrated N-UTC-PD structure, and C is the near-ballistic UTC-PD (NBUTC-PD) structure [14]–[16]. As compared to device A, we can clearly see that there is an additional n- and p-type charge layer in the collector layer of the N-UTC-PD and NBUTC-PD, respectively. Tables I to III show details of the epitaxial layer structure, including the thickness and doping density of devices A, B and C. Fig. 2 shows the

[1]Synopsys, Inc., 700 East Middle field Rd., Mountain View, CA, 94043-4033, U.S.A.

TABLE II
EPI-LAYER STRUCTURE OF DEVICE B: N-UTC-PD

	B. N-UTC-PD			
	Material	Thickness (Å)	Doping Level (/cm3)	Type
Graded P-Contact layer	$In_{0.8}Ga_{0.2}As$	100	5.0E+19	p^{++}
P-Contact layer	$In_{0.53}Ga_{0.47}As$	200	2.0E+18	p^{+}
Diffusion Block layer	$In_{0.52}A_{10.29}Ga_{0.19}As$	200	2.0E+18	p^{+}
Absorption layer	$In_{0.53}Ga_{0.47}As$	1500	5E+19 (top) to 5E+17 (bottom)	p^{+}
Collector layer	InP	200	2.0E+16	N_{-}
N-Charge layer	InP	70	4E+17	N
Collector layer	InP	1330	2.0E16	N_{-}
N Contact layer	InP	7000	5.0E+19	N++
Semi-Insulating InP Substrate	InP			

TABLE III
EPI-LAYER STRUCTURE OF DEVICE C: NBUTC-PD

	C. NBUTC-PD			
	Material	Thickness (Å)	Doping Level (/cm3)	Type
Graded P-Contact layer	$In_{0.8}Ga_{0.2}As$	100	5.0E+19	p^{++}
P-Contact layer	$In_{0.53}Ga_{0.47}As$	200	2.0E+18	p^{+}
Diffusion Block layer	$In_{0.52}A_{10.29}Ga_{0.19}As$	200	2.0E+18	p^{+}
Absorption layer	$In_{0.53}Ga_{0.47}As$	1500	5E+19 (top) to 5E+17 (bottom)	p^{+}
Collector layer	InP	1400	2.0E+16	N_{-}
Charge layer I	InP	100	1.4E+18	P+
Charge layer II	InP	50	2.6E16	P-
Collector layer	InP	50	6.0E18	N
N Contact layer	InP	7000	5.0E+19	N++
Semi-Insulating InP Substrate	InP			

simulated band diagrams of these three devices. As can be seen in device B, the n-type charge layer inserted near the junction of the absorption and collector layers (specified as junction AC in this figure), induces a more significant electron potential drop as compared to that of device A or C. This can effectively suppress the SCS effect [18], which will be discussed later and illustrated in Fig. 3. However, such a high electric (E)-field in or around the AC junction of the N-UTC-PD might lead to a significant electron inert-valley scattering effect and degradation in the transit time limited bandwidth. In order to avoid the problem, as shown in Table II, the high E-field region around the AC junction is as thin as around 20 nm, thinner than the electron mean free path (~82 nm) in the InP collector. This number is calculated using the reported electron effective mass (0.08 m_0), thermal velocity (3.9×10^5 m/s), and mobility (~0.46 m^2/V·s) in the InP layer [25]. In addition, this high E-field will be minimized by the electron induced SCS effect under dynamic operation with a high output photocurrent density [18], which will be discussed later. In contrast to the working principles of device B with the n-type charge layer, in device C (NBUTC-PD [14]–[16]) a p-type charge layer is utilized to minimize the high E-field

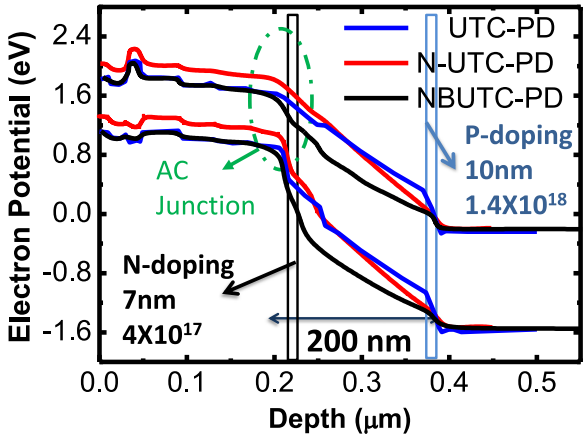

Fig. 2. Simulated band diagrams of UTC-PDs, N-UTC-PDs (n-type charge layer), and NBUTC-PDs (p-type charge layer) under the same reverse bias (−1 V). The position of the AC junction is specified.

inside the collector and sustain the over-shoot drift-velocity of the electrons.

Nevertheless, a larger reverse bias voltage (−2 versus −1 V) is usually necessary compared with that of devices A and B, to overcome the SCS effect [16]. This would increase the probability of the miniaturized THz NBUTC-PD suffering from thermal failure under high-power operation [16], [23]. Fig. 3(a)–(c) show the simulated E-field distributions of devices A to C, respectively, under static (no light illumination) and dynamic operations. The E-field simulation is obtained using the same software for calculating the band diagram (see Fig. 2).

The three simulated devices have the same active diameter (3 μm) and collector layer thickness (~200 nm); see Tables I to III. In our simulations, it is assumed that these devices are operated under the same reverse bias (−1 V), load resistance (50 Ω), and output photocurrent (14 mA). Here, the –1V bias is chosen for simulation due to the fact that this value is close to the reported optimum bias of UTC-PDs for THz applications [10]. As shown in Fig. 3(b), by inserting the n-type charge layer in the collector of the N-UTC-PD, the static E-field (indicated by the blue open symbols), under −1 V bias will be the highest in the AC-junction. This is used to compensate the strong space-charge induced field (SCS; red line with solid symbol on this figure) under high power operation. Under dynamic operation with a 14 mA average output photocurrent flowing through a 50 Ω load, the effective dc reverse bias into the devices should be reduced from −1 to around −0.3 V. The corresponding quasi-static E-field is indicated by the black trace with open symbols in this figure. The electron induced SCS field (E_{SCS}) is further subtracted from the effective dc bias (−0.3 V) E-field to produce the net E-field inside the collector layer, shown as a red trace with open symbols (14 mA; Net) in the figure. The formula used for the calculation of E_{SCS} for different positions in the collector layer is as follows [18]:

$$E_{\mathrm{scs}}(x) = J\left(\frac{x}{\varepsilon V_e}\right) \tag{1}$$

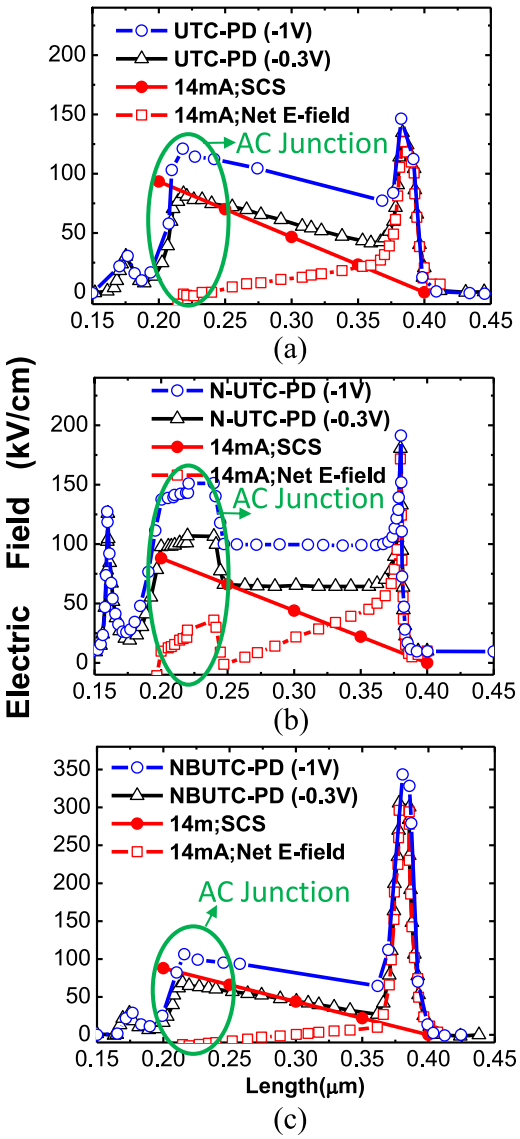

Fig. 3. The simulated E-fields in the (a) UTC-PD, (b) N-UTC-PD, and (c) NBUTC-PD collectors under −1 V bias. Blue lines: static (dark) E-field under −1 V. Black lines: quasi-static E-field under 14 mA photocurrent (−0.3 V effective bias). Red lines: space-charge screening (SCS) induced E-field (closed circles) and net E-field (open squares) under 14 mA photocurrent. The position of the AC junction in each device has been specified.

where x indicates a distance that varies from 200 nm at the absorption-collector (AC) junction to zero at the collector and sub-collector (n^+ InP) junction; J is the output photocurrent density; ε is the dielectric constant of InP; and V_e is the drift-velocity of electrons inside the InP collector layer. Although equation (1) is based on a static model, it can also provide a reasonable approximation for the device dynamic response when the modulation frequencies are much lower than the carrier-transit-limiting bandwidth (f_T) [18]. The value of f_T in considered here is much larger than the measured net device O-E bandwidths (∼0.3 THz). This has been verified by performing the equivalent-circuit modeling technique onto our devices [15], [16], [26] and will be discussed latter in the next section about measurement results.

We can thus conclude that equation (1) is suitable for the analysis for dynamic SCS effect within the frequency range of interest (O-E bandwidth; dc to 0.3 THz). In addition, we assume a constant electron drift-velocity ($\sim 4 \times 10^7$ cm/s) [18], [26] in the calculation for E_{scs}. Although an E-field dependent carrier drift-velocity might be necessary for a rigorous simulation, such as Monte Carlo (MC) technique [27], the assumption of a constant electron drift-velocity here can still provide reasonable accuracy. This is because that our InP collector layer thickness (∼200 nm) is larger than that of electron mean free path in InP (∼82 nm) [25]. According to the MC simulation result, for the ∼200 nm thick InP based collector layer, the simulated electron drift-velocity is nearly constant and ranges between $4 \sim 6 \times 10^7$ cm/s [27].

Since the three devices (A, B, and C) being compared have the same collector layer thickness (∼200 nm), the same active area (diameter of mesa), and operate at the same output photocurrent (∼14 mA), they should have the same traces of E_{SCS} as indicated by the closed red symbols (14 mA; SCS) in Fig. 3. Under dynamic operation, there is no net E-field, which is completely screened by the SCS effect and the opposite polarity of photocurrent (14 mA) induced voltage on the 50 Ω load, in the AC junction of UTC-PD and NBUTC-PD. This indicates that the slow diffusion of electrons from the p-type photo-absorption layer cannot be accelerated in the collector layer. There is thus a serious degradation in the electron transit time limited bandwidth and saturation of the output power with a 14 mA output photocurrent. One effective way to overcome the above-mentioned problem in UTC-PDs and NBUTC-PDs is to further increase the reverse bias voltage. For NBUTC-PDs with a 200 nm thick collector layer, the optimum bias for THz operation is usually located at −2 V [15], [16]. However, high bias induced thermal failure tends to occur in cases with a miniaturized NBUTC-PD [16], [23].

On the other hand, for the N-UTC-PD, we can clearly see that the high E-field (∼150 kV/cm) at the AC junction will be screened and reduces to 10–37 kV/cm. This value is still strong enough to accelerate the slow diffusion of electrons from the p-type absorption layer and minimize degradation in the internal carrier transit time. From the simulation results shown in Figs. 2 and 3, we can conclude that compared with the UTC-PD and NBUTC-PD, our proposed N-UTC-PD structure with the n-type charge layer near the AC junction can effectively suppress the SCS effect under a moderate reverse bias (around –1 V). This would minimize the probability of a miniaturized THz PD suffering from thermal failure under high-power operation. In this study, using an advanced flip-chip bonding package as discussed latter, we are able to successfully demonstrate ultrafast speed with high-power performance of this N-UTC-PD in the THz regime (∼300 GHz).

Fig. 4 shows the top-view of the active PD chip, CPW pad on the AlN substrate for flip-chip bonding, and the PD chip after flip-chip bonding. Here two different kinds of flip-chip bonding structures (labeled A and B) are implemented, as shown in Fig. 4(a) and (b), for optimum frequency response performance at the J-(220–325 GHz) and D-bands (110–170 GHz), respectively. The epi-layer structure of our fabricated N-UTC-PD

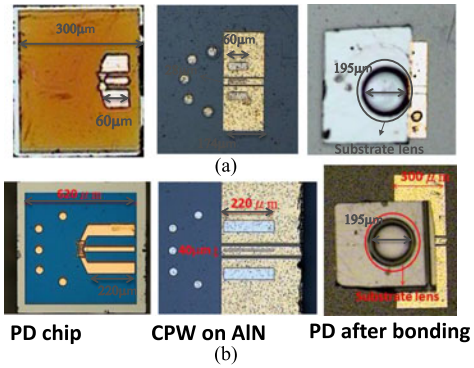

Fig. 4. Top-views of active N-UTC-PD chips, bonding pads on AlN substrate, and PD chip after flip-chip bonding of structures A (a) and B (b).

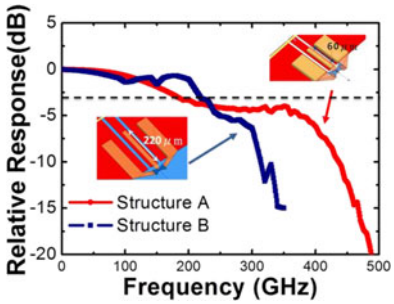

Fig. 5. The simulated S_{12} frequency responses of structures A and B; the inset shows the geometric structure used for high-frequency simulation. For clarity, the AlN and InP substrates are both assumed to be transparent.

is identical to that shown in Table II, with the exception in the charge layer doping density. We increase the n-type charge layer doping density from 4 to 8.3$\times$ 10^{17} cm^{-3} in order to achieve pronounced bias modulation characteristic of photo-generated MMW power [28] and its simulated saturation output current is about $\sim$11 mA. Such value is obtained through the use of the proposed E-field simulation method as discussed in Fig. 3. The fabricated device has a diameter of $\sim$3 μm and its measured dc responsivity is $\sim$0.1 A/W, which is larger than the values reported for ultrafast UTC-PDs with a close 3-dB O-E bandwidth ($\sim$170 GHz with 0.03 A/W responsivity) [12].

Fig. 5 shows the simulated MMW frequency response of the transmission coefficient (S_{12}) of the newly designed flip-chip bonding structure (structure A) and the reference structure based on our previous design (structure B) [16] for J- and D-band operation, respectively. The insets show the two device structures A and B used for high-frequency simulation. Here, in our simulation, the active PD is assumed to be an ideal current source with an infinitely large 3-dB bandwidth and the MMW transmission represents the photo-generated MMW power transferred from the active PD mesa (port 2) through the bonding pedestals to the CPW pads (port 1) on the AlN substrate. In order to minimize the high-frequency roll-off of the packaged PD chip and improve device heat-sinking, we let the position of the Au/Sn solder bump be as close as possible to the active PD mesa [16] in both structures A and B. Furthermore, by properly adjusting the size of the CPW lines on the AlN substrate, we can manipulate the optical-to-electrical (O-E) frequency response of the flip-chip packaged PD module. Structure B exhibits a broad

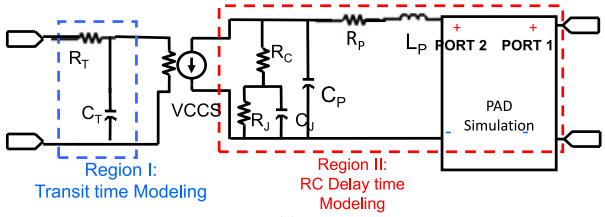

(a)

	Physical Meaning	Structure A	Structure B
Cj	Junction Capacitance (fF)	4	5.1
Rj	Junction Resistance (kΩ)	>100	>100
Rp	Parasitic Resistance (Ω)	1	1
Rc	Contact Resistance (Ω)	100.5	95
Cp	Parasitic Capacitance (fF)	1.12	1.12
Lp	Parasitic Inductance (pH)	0.05	0.05
PAD Simulation	The simulated S-parameters for PAD by using HFSS software		

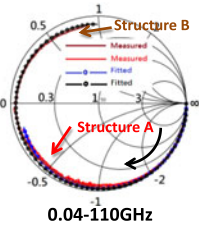

(b)

Fig. 6. (a) Equivalent-circuit-model. VCCS: voltage controlled current source; (b) Measured (continuous line) and fitted (open circles) S_{11} parameters from near dc to 110 GHz under a fixed dc bias (-2 V). The head of the black arrow indicates the increase in the sweep frequency. The inserted table shows the values of the circuit elements used in the modeling process.

frequency response with a 3-dB bandwidth at around 230 GHz (from dc). In order to further extend the O-E bandwidth, the areas of the bonding pad and the Au/Sn bumps in structure A are both reduced and it can sustain a flat O-E response (with a 4 dB bandwidth at $\sim$350 GHz) when the operating frequency reaches nearly 400 GHz. Such bandwidth is capable of covering the entire J-band. Although structure A has a much higher bandwidth, structure B exhibits a larger magnitude of response in the 130 to 230 GHz frequency range. This is the advantage of structure B for dc to D-band applications.

To verify the accuracy of the design discussed above, measurement and analysis of the MMW reflection coefficients (S_{11}; from near dc to 110 GHz) is performed on real packaged PDs, as shown in Fig. 4. Here, we use the two-port equivalent-circuit-model [15], [16], [26], which includes two bandwidth-limiting factors (i.e., carrier transit time (T_t) and RC delay time (T_{RC})) [15], [16], [26], as shown in Fig. 6(a), to fit the measured S_{11} parameters. In such model, the "pad simulation block" is just the simulation result what we have discussed in Fig. 5. The fitted values of each circuit element, except for R_T and C_T, are shown in the Table inserted into Fig. 6(b). During our device modeling process for the extraction of extrinsic f_{RC} of active PD dies, such two artificial circuit elements (R_T and C_T) have been removed due to that they are used to mimic the low-pass frequency response of internal carrier transient time [15], [26]. Fig. 6(b) shows the measured and simulated frequency responses for the S_{11} reflection coefficient parameter under a bias voltage of -2 V bias for structures A and B; see the Smith chart. Both structures (A and B) were packaged with the active N-UTC-PDs with the same active diameter of 3 μm for fair comparison. Clearly, the simulated and measured results for both structures match very well, from 40 MHz to 110 GHz, and the extracted extrinsic RC parameters for these two active PDs are also very close because both devices share the same epi-layer structures and active diameters.

As can be seen, although both packaged structures (A and B) have the same active PD size, the structure B trace (on the Smith chart) is longer than that of structure A. The results indicate that the MMW signal for structure B suffers from a larger phase-shift and more serious high-frequency roll-off; see Fig. 5. Furthermore, from this we can understand that not only the active PD itself but also the flip-chip bonding structure plays an important role in determining the net O-E bandwidth of a packaged PD module operating in the THz regime.

III. Measurement Results and Discussion

A heterodyne beating system is used to measure the dynamic performance of the fabricated device structure. A power meter with two different sensor heads (dc to 50 and 75–110 GHz) is used for measurement in the range from dc to 110 GHz. When the measurement frequency is greater than 110 GHz, a thermal MMW power meter (PM4, VDI-Erickson) is used. The maximum measurement bandwidth for our system is limited by our WR-3.4 waveguide based MMW probe operating at 325 GHz. All the dynamic measurement results presented here, which include the O-E frequency responses and THz output power, have been carefully de-embedded to remove any contributions due to losses from the passive components used. From dc to 50 GHz, the frequency dependent loss of passive components mainly originates from the radio-frequency (RF) coaxial cable and bias tee, typically around 8 dB at 50 GHz operation. This value of frequency dependent loss has been carefully verified by use of a broadband network analyzer (0.01 to 67 GHz). When the measurement frequency further increases (75–325 GHz), there are three major sources of insertion loss in our setup. The first is the frequency dependent insertion loss of the waveguide probe. For the case of WR-3.4 waveguide probe, its loss is around 5 dB at 280 GHz operation. This value is provided by the manufacturer of the waveguide probe.[2] The second is the loss associated with the straight WR-10 waveguide section (0.55 dB at 280 GHz),[3] which is connected with the power sensor head. The last is from the waveguide taper (0.3 dB at 280 GHz).[3] This component connects the WR-10 waveguide and the head of the waveguide probes (WR-3.4 or WR-6). After our calibration procedures, the corrected values of measured power matches well at the edged frequency of different bands, which include 50, 75, 110, 170, and 220 GHz. This reveals the accuracy of our calibration procedures.

Fig. 7(a) and (b) show the measured bias dependent optical-to-electrical (O-E) frequency responses of the proposed N-UTC-PD with a 5 μm active diameter and flip-chip bonding package structure B from the near dc to 300 GHz under two different output photocurrents at 3 and 5 mA, respectively. Here, we define our 3-dB bandwidth by use of the measured power from our device at 0.5 GHz as dc reference point. As shown in Fig. 7(a), at a lower output photocurrent (3 mA) the speed performance is insensitive to the bias voltage, with a maximum 3-dB bandwidth of ~170 GHz. On the other hand, as shown in Fig. 7(b), when the output photocurrent reaches 5 mA, a much less high-frequency roll-off is observed under optimum bias at −1 V and

[2]GGB Industries, Inc., P.O. BOX 10958, NAPLES, FL 34101.

[3]Virginia Diodes, Inc., 979 Second Street, S.E. Suite 309, Charlottesville, VA 22902-6172. VDI APPLICATION NOTE: Power Measurement above 110 GHz.

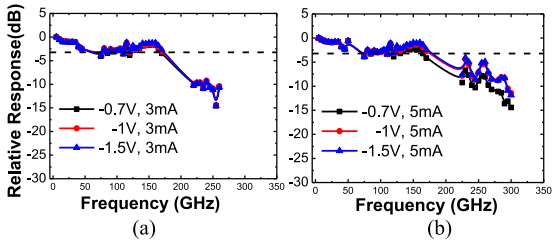

Fig. 7. Bias dependent O-E frequency responses measured under different output photocurrents: (a) 3 mA and (b) 5 mA for structure B with the 5 μm active diameter of PD.

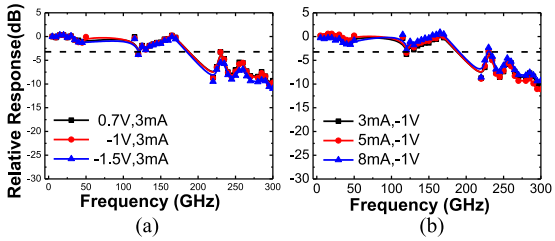

Fig. 8. (a) Bias dependent O-E frequency responses measured at a fixed output photocurrent of 3 mA; and (b) O-E frequency responses measured at different photocurrents (3, 5, and 8 mA) under the optimum bias of –1 V for structure B with a 3 μm active diameter of PD.

the measured 3-dB bandwidth is nearly 225 GHz. This is close to our simulation result, as illustrated in Fig. 5.

A significant enhancement in speed is observed with an increase in the output photocurrent density usually observed in UTC-PDs which can be attributed to the self-induced field in the p-type absorption layer [9], [29] and the moderate electron induced SCS effect in the collector layer [26]. Here, the strong output photocurrent density of our miniaturized device would result in an additional drop in the electron potential in the p-type absorption layer which could accelerate the electron diffusion process [9], [29]. Furthermore, the high-current induced SCS effect at the AC junction can reduce the strong static E-field and minimize the inter-valley scattering effect of the drift-electrons, which would result in the observed bandwidth enhancement [26].

Fig. 8(a) shows the measured O-E frequency responses of a PD. The flip-chip bonding package (structure B) is the same but with a smaller active diameter (~3 μm) and an output photocurrent of 3 mA. Compared with the measurement results obtained with the same output photocurrent (3 mA) as shown in Fig. 7(a), we can clearly see a significant enhancement in bandwidth (170 to near 230 GHz). This is due to the increase in the output photocurrent density (15.3 to 42.4 kA/cm^2). Fig. 8(b) shows the measured O-E frequency responses of the packaged device with a 3 μm active diameter for different output photocurrents (3, 5, and 8 mA) and under an optimum bias voltage (−1 V). As can be seen, the measured O-E frequency response has a maximum 3-dB bandwidth at around ~230 GHz, which is close to the measurement results for the PD with a 5 μm active diameter, as shown in Fig. 7(b). This result implies that the flip-chip bonding structure is the major bandwidth limiting factor for the full packaged module with the miniaturized PD (< 5 μm active diameter). There is also a significant enhancement in the output

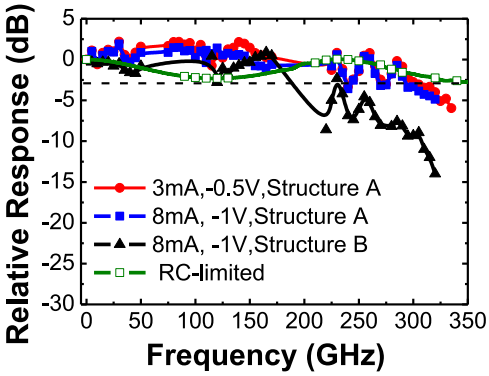

Fig. 9. The O-E frequency responses of structures A and B measured under different bias voltages and output photocurrents. The active diameter of the packaged PD is 3 μm.

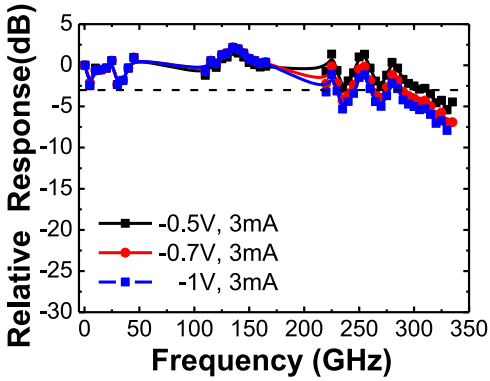

Fig. 10. The bias dependent (−0.5, −0.7, and −1 V) O-E frequency responses of structure A with a 3 μm active diameter of PD measured at 3 mA output photocurrent.

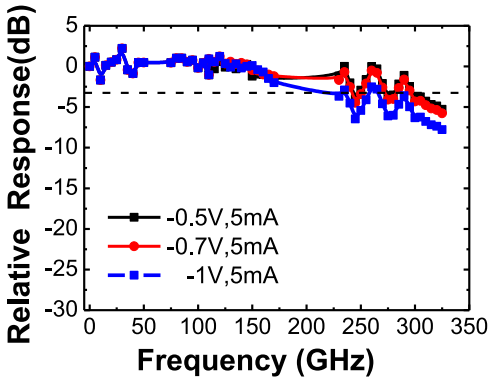

Fig. 11. The bias dependent (−0.5, −0.7, and −1 V) O-E frequency responses of structure A with a 3 μm active diameter of PD measured at 5 mA output photocurrent.

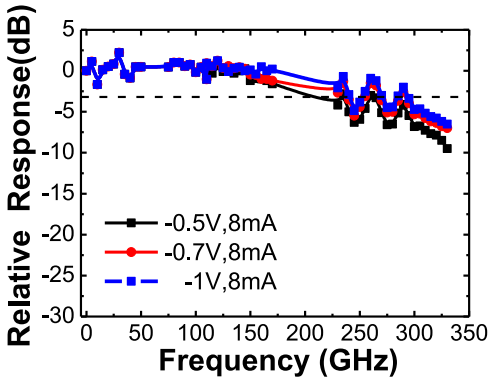

Fig. 12. The bias dependent (−0.5, −0.7, and −1 V) O-E frequency responses of structure A with a 3 μm active diameter of PD measured at 8 mA output photocurrent.

MMW power in the frequency range of 110–170 GHz (D-band), which is consistent with the simulation results shown in Fig. 5.

Fig. 9 shows the measured O-E frequency responses for the 3 μm active diameter PD flip-chip bonded package fabricated with structures A and B obtained under different operating conditions. There is much less serious high-frequency (220–325 GHz) roll-off in the O-E frequency response for structure A than for structure B under the same operating conditions (8 mA photocurrent and under a –1 V bias). The measurement results clearly match the simulation results, as shown in Fig. 5, verifying the accuracy of our proposed approach for PD simulation. In addition, we can obtain a measured O-E frequency response with the maximum 3-dB bandwidth as high as 305 GHz for structure A under optimum operating conditions (3 mA; −0.5 V). By using the established equivalent circuit-model, as discussed in Figs. 5 and 6, we can further extract the RC-limited frequency response of our demonstrated device, which is shown as green trace with open symbol in this figure. The RC-limited 3-dB bandwidth (∼350 GHz) is very close with the measured net O-E bandwidth (305 GHz). This represents that the carrier transit time limited bandwidth is much larger than the net O-E bandwidth and proves the validity of using equation (1) in the discussions for Fig. 3.

We further examine the ultrafast carrier dynamic of packaged N-UTC-PDs fabricated with flip-chip bonding structure A, with a 3 μm diameter of active PD under high-power operation. Figs. 10–12 show the measured bias dependent O-E frequency responses of structure A under output photocurrents of 3, 5, and 8 mA, respectively. As can be seen in Fig. 10, under a low output photocurrent (3 mA), the optimum bias for maximum speed (315 GHz 3-dB bandwidth) performance occurs at −0.5 V. As shown in Fig. 12, when the output photocurrent reaches 8 mA, in order to compensate for the electron induced SCS effect, the optimum bias shifts to −1 V and there is a slight degradation in the 3-dB bandwidth to 290 GHz. The optimum bias is very close to that of the THz UTC-PD module with the integrated bow-tie antenna that operates at the 250 GHz frequency [10]. The achieved maximum 3-dB bandwidth here (∼315 GHz) is higher than the number (∼310 GHz) reported for the fastest UTC-PD [11] under a much smaller load resistance (12.5 versus 50 Ω) and with a smaller responsivity than that of ours (<0.07 versus 0.1 A/W).

Fig. 13 shows the measured photo-generated MMW power versus output photocurrent for structure A under different reverse biases by using our two-laser heterodyne-beating setup. In order to obtain the maximum output power from our PD module, the measurement frequency is fixed at 285 GHz, which corresponds to the resonant peak frequency in the measured O-E frequency responses, as shown in Fig. 12.

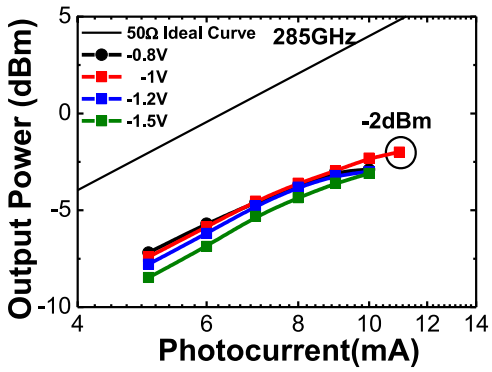

Fig. 13. The measured photo-generated MMW power versus photocurrent of structure A with a 3 μm active diameter of PD under sinusoidal signal excitations and different reverse biases at an operating frequency of 285 GHz. The solid line shows the ideal trace for a 100% modulation depth and 50 Ω load.

The ideal relation between the MMW power and averaged photocurrent (solid line) with a 100% optical modulation depth under a 50 Ω load is also plotted for reference. We can clearly see that under the optimum bias (−1 V), the saturation current is around 11 mA with a −2 dBm maximum output power. Such value of saturation current is consistent with our E-field simulation results of device with a $8.3\times\ 10^{17}$ cm^{-3} n-type charge layer doping density inside its collector layer, as discussed in Fig. 3. The increase in the reverse bias voltage (−1 to −1.2 V) leads to degradation in the saturation current (11 to 10 mA) and power (−2 to −3.1 dBm), possibly attributable to device heating or the inter-valley scattering effect which induces degradation in the electron drift-velocity [10], [15]. As compared to the reported output power (0.9 dBm) at 300 GHz operating frequency from a high-performance dual UTC-PDs integrated with a power combing circuit and excited by the same two-laser heterodyne-beating setup [13], our achieved output power (−2 dBm) from a single device here is considered high and can as be further improved by using the power combing technique.

In order to further boost the output power and minimize the device heating under high power operation, an optical pulse train system with a repetition rate in the MMW regime is introduced for CW photonic high-power generation [21]–[24], [30]. Optical short pulse trains offer high peak intensities for efficient excitation of the CW THz signal while the low duty cycle (the ratio of the pulse duration over the pulse period) minimizes the device heating. Moreover, the broad spectral bandwidth required for short optical pulses has been found beneficial in providing higher spectral beat strength at the CW THz signal frequency under consideration [21]. Fig. 14(a) shows the measured photo-generated MMW power versus output photocurrent observed under different reverse biases and optical short pulse train excitations with a repetition rate fixed at 280 GHz. The optical pulse train generator is comprised of a dual-drive intensity modulated frequency comb and an optical line-by-line pulse shaper; for more details please see Ref. [23].

The transform-limited pulse train at 20 GHz is amplified by an erbium-doped fiber amplifier and delivered to a dispersion-decreasing fiber for soliton pulse compression down to 300 fs. The resulting soliton compressed spectrum is then delivered to

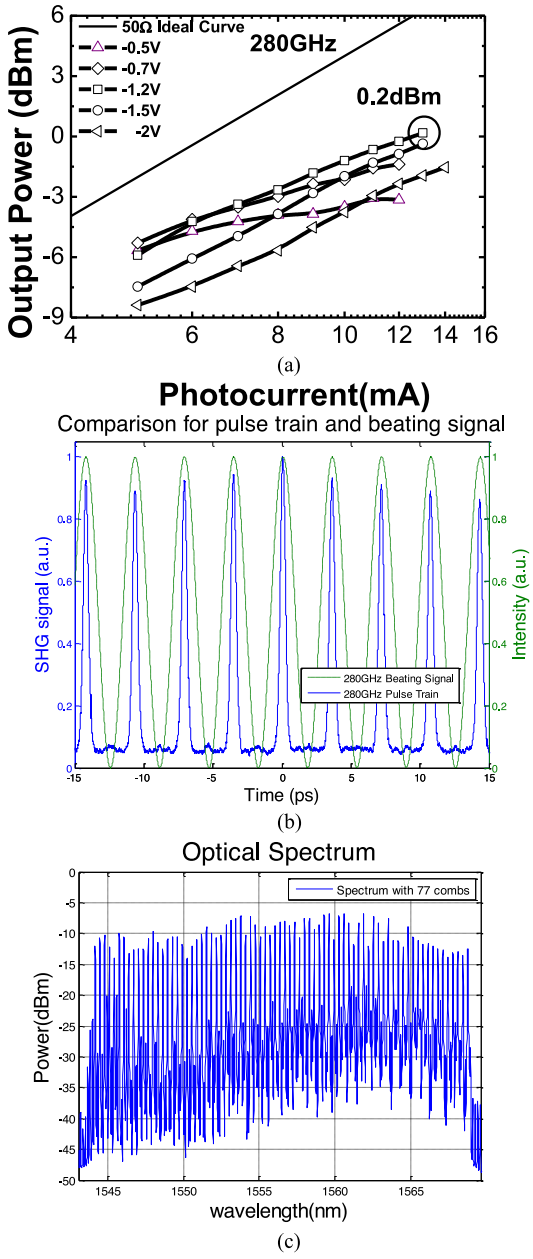

Fig. 14. (a) The measured photo-generated MMW power versus photocurrent of structure A with a 3 μm active diameter of PD under pulse train signal excitations and different reverse bias at 280 GHz operation frequency. Solid line is ideal trace for 100% modulation depth and 50 Ω load. (b) Intensity autocorrelation traces of the sinusoid and pulse train. (c) Corresponding spectrum for the 280 GHz pulse train.

a home-made line by line pulse shaper, where periodical spectral phase control is applied to achieve pulse train repetition-rate multiplication from 20 to 280 GHz [22]. This operation is commonly known as temporal Talbot self-imaging [31]. The intensity autocorrelation traces for the optical sinusoid (dashed line) and the 280 GHz pulse train (solid line) are provided in Fig. 14(b). The optical spectrum filtered by the pulse shaper is shown in Fig. 14(c). Compared with under sinusoidal signal excitation, as shown in Fig. 13, the optimum bias for maximum output power slightly increases to −1.2 V and the bias

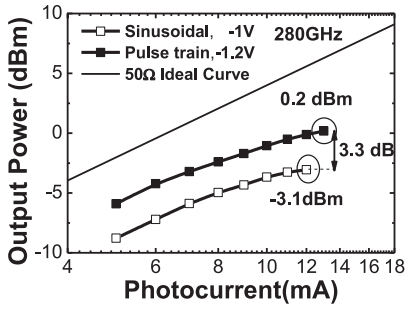

Fig. 15. The measured photo-generated MMW power of structure A with a 3 μm active diameter of PD versus photocurrent under sinusoidal (open symbol) and pulse train (close symbol) excitations at 280 GHz operation frequency. Solid line is ideal trace for 100% modulation depth and 50 Ω load.

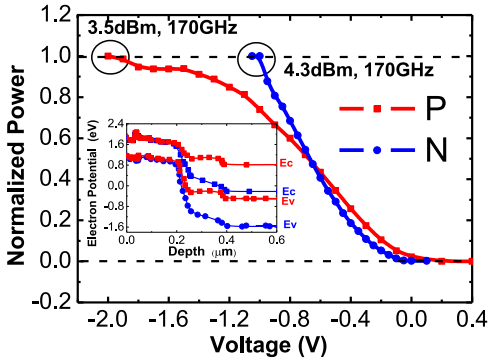

Fig. 16. The measured transfer curve (bias voltage versus output MMW power) at 170 GHz of the N-UTC-PD (-N) and NBUTC-PD (-P). Both devices have the same active diameter (3 μm) and are packaged with structure B. The insets show the simulated band diagram of the N-UTC-PD under zero (red lines) and −1 V bias (blue line).

dependent performance becomes more distinct under pulse excitation. Such phenomenon is understood as a higher bias voltage is usually required to compensate the higher peak space-charge field induced by the injected optical short pulses, thus leading to a higher sensitivity of device's dynamic behavior to the reverse bias [21]. Furthermore, by using short pulse excitation, a significant enhancement in output power and saturation current can be observed. Although compared with the two-laser heterodyne-beating approach operated at the same frequency (280 GHz), the proposed optical pulse train excitation should contain the additional component of power at higher harmonic frequency (560, 840 GHz, etc.). This should not be an issue in our measurement due to the fact that our device under test (DUT) and MMW probe both have cut-off frequency at around ∼300 GHz and the contribution from these harmonic terms (above 560 GHz) in the measured THz power are fully suppressed.

Fig. 15 shows the detail comparison of output power performance between sinusoidal and short pulse operations of the same PD module (structure A) under the same operating frequency (280 GHz) and optimum bias. As can be seen, compared with under sinusoidal operation, optical short-pulse train can offer ∼3 dB enhancement in output power under the same output photocurrent. This corresponds to that the effective modulation depth can be increased from 60% to 84% for sinusoidal and pulse operations, respectively. The maximum output sub-THz power can reach 1.04 mW (13 mA saturation current) at 280 GHz operation. Such number is comparable with the reported maximum output power (1.2 mW) from a state-of-the-art photomixer module, which is composed of dual UTC-PDs and a power combing circuit with a limited fractional bandwidth (∼70 GHz; 280 to 350 GHz) operated at 300 GHz central frequency [13]. To the best of author's knowledge, by using the established optical short pulse train generator as optical source for our PD excitation, the measured output power here is the highest value (under continuous wave operation) ever reported for photonic generation of THz-wave from a single ultrafast PD at 300 GHz frequency regime [10]–[12], [16].

As compared to the reported power enhancements of effective modulation depth at lower frequency range (100 to 160 GHz) [21], [23], the current value is slightly degraded. We attribute the observed degradation to two potential factors: (1) As compared to Ref. [23], our current intensity autocorrelation traces (solid blue trace in Fig. 12(b)) shows a roughly 12% peak amplitude variation. This means not all of the optical power is used to contribute to the excitation of 280 GHz electrical signal. (2) The power enhancement is moderately sensitive to the optical waveform. The theoretical prediction of 6-dB enhancement was derived assuming all frequency components have equal amplitude ($sinc^2$ temporal intensity profile) [21]. Here, our pulse is derived using soliton propagation in the dispersion-decreasing fiber, and the resulting pulse intensity takes on a $sech^2$ profile.

The fast bias modulation characteristic of high-power PD is important for the application of photonic wireless communication especially for the case of short-pulse train excitation [32]. By use of bias modulation technique onto PD for remote-up conversion, the direct on-off keying (OOK) modulation of optical pulse train can be eliminated. This would solve the problem in serious chromatic dispersion of modulated optical pulse train during fiber transmission [32]. However, the near forward bias operation of UTC-PD is necessary to quench the photo-generated THz power, which would seriously limit its modulation speed [28]. In our previous work, we have demonstrated that by incorporation an additional p-type charge layer inside collector of UTC-PD (NBUTC-PD), the operation window would be shifted to reverse bias regime and ultra-fast bias modulation performance (>25 Gb/s) for photonic wireless communication has been demonstrated [33]. Fig. 14 shows the measured transfer curve (bias voltage versus photo-generated MMW power in linear scale) of NBUTC-PD and N-UTC-PD at 170 GHz operating frequency. Each trace is normalized to the value of its maximum output power, which is specified on such figure. Both devices have the same active diameter (3 μm), flip-chip bonding structure (structure B), and absorption/collector layer thicknesses (150/∼200 nm) for fair comparison. We can clearly see that the N-UTC-PD has a similar swinging range (∼ +4 to around −25 dBm; noise floor of our measurement system) of MMW power with that of NBUTC-PD but a much smaller driving voltage (1 versus ∼1.6 V). Such significant bias dependent performance in MMW power of the N-UTC-PD is mainly due to the insertion of the n-type charge layer inside the collector. The inset to Fig. 16 shows a simulated band diagram[1] of our proposed N-UTC-PD structure under zero and −1 V bias

voltages. This simulation results clearly indicate that the photo-generated MMW power could be quenched at zero-bias due to the un-depleted collector layer.

IV. Conclusion

In this paper we demonstrated a novel collector design and package structure designed to further improve the high-power performance of the UTC-PD. Through the use of an advanced flip-chip bonding package, the device exhibits an extremely wide O-E bandwidth ($\sim$315 GHz) and reasonable responsivity (0.1 A/W). Detailed dynamic analysis of the device package at different photocurrents and reverse bias voltages suggests that non-equilibrium electron transport plays an important role in determining the maximum output power in the THz regime. By using a femto-second optical short pulse train as a light source to minimize device heating and further enhance photo-generated THz power, a record-high CW output power from a single PD (1.04 mW) at an $\sim$300 GHz frequency regime has been successfully demonstrated. The proposed device structure also exhibits excellent bias modulation characteristics, i.e., extremely small driving voltage (0 to –1 V) with $>$ 30 dB swing of sub-THz power.

References

[1] V. J. Urick, J. F. Diehl, J. M. Singley, C. E. Sunderman, and K. J. Williams, "Long-reach analog photonics for military applications," *Opt. Photon. News*, vol. 25, pp. 38–43, Oct. 2014.

[2] Z. Popović and E. N. Grossman, "THz metrology and instrumentation," *IEEE Trans. Terahertz Sci. Technol.*, vol. 1, no. 1, pp. 133–144, Sep. 2011.

[3] S. Koenig, D. Lopez-Diaz, J. Antes, F. Boes, R. Hennberger, A. Leuther, A. Tessmann, R. Schmogrow, D. Hillerkuss, R. Palmer, T. Zwick, C. Koss, W. Freude, O. Ambacher, J. Leuthold, and I. Kallfass, "Wireless sub-THz communication system with high data rate," *Nature Photon.*, vol. 7, pp. 977–981, Dec. 2013.

[4] J.-W. Shi, C.-B. Huang, and C.-L. Pan, "Millimeter-wave photonic wireless links for very-high data rate communication," *NPG Asia Mater.*, vol. 3, no. 2, pp. 41–48, Apr. 2011.

[5] H.-J. Song and T. Nagatsuma, "Present and future terahertz communications," *IEEE Trans. Terahertz Sci. Technol.*, vol. 1, no. 1, pp. 256–263, Sep. 2011.

[6] G. Ducournau, P. Szriftgiser, A. Beck, D. Bacquet, F. Pavanello, E. Peytavit, M. Zaknoune, T. Akalin, and J.-F. Lampin, "Ultrawide-bandwidth single-channel 0.4-THz wireless link combining broadband quasi-optic photomixer and coherent detection," *IEEE Trans. Terahertz Sci. Technol.*, vol. 4, no. 3 pp. 328–337, May, 2014.

[7] T. Nagatsuma, M. Shinagawa, N. Sabri, A. Sasaki, Y. Royter, and A. Hirata, "1.55-μm photonic systems for microwave and millimeter-wave measurement," *IEEE Trans. Microw. Theory Technol.*, vol. 49, no. 10, pp. 1831–1839, Oct. 2001.

[8] Y. Li, A. Rashidinejad, J.-M. Wun, D. E. Leaird, J.-W. Shi, and A. M. Weiner, "Photonic generation of W-band arbitrary waveforms with high time-bandwidth products enabling 3.9 mm range resolution," *Optica*, vol. 1, no. 6, pp. 446–454, Dec. 2014.

[9] H. Ito, S. Kodama, Y. Muramoto, T. Furuta, T. Nagatsuma, and T. Ishibashi, "High-speed and high-output InP-InGaAs unitraveling-carrier photodiodes," *IEEE J. Sel. Topics Quantum Electron.*, vol. 10, no. 4, pp. 709–727, Jul./Aug. 2004.

[10] T. Ishibashi, Y. Muramoto, T. Yoshimatsu, and H. Ito, "Unitraveling-carrier photodiodes for terahertz applications," *IEEE J. Sel. Topics Quantum Electron.*, vol. 20, no. 6, p. 3804210, Nov./Dec. 2014.

[11] H. Ito, T. Furuta, S. Kodama, N. Watanabe, and T. Ishibashi, "Inp/InGaAs uni-travelling-carrier photodiode with 310GHz bandwidth," *Electron. Lett.*, vol. 36, no. 21, pp. 1809–1810, Oct. 2000.

[12] H. Ito, T. Furuta, F. Nakajima, K. Yoshino, and T. Ishibashi, "Photonic generation of continuous THz wave using uni-traveling-carrier photodiode," *J. Lightw. Technol.*, vol. 23, no. 12, pp. 4016–4021, Dec. 2005.

[13] H.-J. Song, K. Ajito, Y. Muramoto, A. Wakatsuki, T. Nagatsuma, and N. Kukutsu, "Uni-travelling-carrier photodiode module generating 300 GHz power greater than 1 mW," *IEEE Microw. Wireless Components Lett.*, vol. 22, no. 7, pp. 363–365, Jul. 2012.

[14] J.-W. Shi, F.-M. Kuo, C.-J. Wu, C. L. Chang, C. Y. Liu, C.-Y. Chen, and J.-I. Chyi, "Extremely high saturation current-bandwidth product performance of a near-ballistic uni-traveling-carrier photodiode with a flip-chip bonding structure," *IEEE J. Quantum Electron.*, vol. 46, no. 1, pp. 80–86, Jan. 2010.

[15] J.-W. Shi, F.-M. Kuo, and J. E. Bowers, "Design and analysis of ultra-high speed near-ballistic uni-traveling-carrier photodiodes under a 50 Ω load for high-power performance," *IEEE Photon. Technol. Lett.*, vol. 24, no. 7, pp. 533–535, Apr. 2012.

[16] J.-M. Wun, C.-H. Lai, N.-W. Chen, J. E. Bowers, and J.-W. Shi, "Flip-chip bonding packaged THz photodiode with broadband high-power performance," *IEEE Photon. Technol. Lett.*, vol. 26, no. 24, pp. 2462–2464, Dec. 2014.

[17] A. S. Cross, Q. Zhou, A. Beling, Y. Fu, and J. C. Campbell, "High-power flip-chip mounted photodiode array," *Opt. Exp.*, vol. 21, no. 8, pp. 9967–9973, Apr. 2013.

[18] K. Kato, "Ultrawide-band/high-frequency photodetectors," *IEEE Trans. Microw. Theory Technol.*, vol. 47, no. 7, pp. 1265–1281, Jul. 1999.

[19] N. Li, X. Li, S. Demiguel, X. Zheng, J. C. Campbell, D. A. Tulchinsky, K. J. Williams, T. D. Isshiki, G. S. Kinsey, and R. Sudharsansan, "High-saturation-current charge-compensated InGaAs-InP uni-traveling-carrier photodiode," *IEEE Photon. Technol. Lett.*, vol. 16, no.3, pp. 864–866, Mar. 2004.

[20] M. Chtioui, A. Enard, D. Carpentier, S. Bernard, B. Rousseau, F. Lelarge, F. Pommereau, and M. Achouche, "High-performance uni-traveling-carrier photodiodes with a new collector design," *IEEE Photon. Technol. Lett.*, vol. 20, no. 13, pp. 1163–1165, Jul. 2008.

[21] F.-M. Kuo, J.-W. Shi, H.-C. Chiang, H.-P. Chuang, H.-K. Chiou, C.-L. Pan, N.-W. Chen, H.-J. Tsai, and C.-B. Huang, "Spectral power enhancement in a 100-GHz photonic millimeter-wave generator enabled by spectral line-by-line pulse shaping," *IEEE Photon. J.*, vol. 2, no. 5, pp. 719–727, Oct. 2010.

[22] H.-P. Chuang and C.-B. Huang, "Generation and delivery of 1-ps optical pulses with ultrahigh repetition-rates over 25-km single mode fiber by a spectral line-by-line pulse shaper," *Opt. Exp.*, vol. 18, pp. 24003–24011, 2010.

[23] J.-M. Wun, H.-Y. Liu, C.-H. Lai, Y.-S. Chen, S.-D. Yang, C.-L. Pan, J. E. Bowers, C.-B. Huang, and J.-W. Shi, "Photonic high-power 160 GHz signal generation by using ultra-fast photodiode and a high-repetition-rate femtosecond optical pulse train generator," *IEEE J. Sel. Topics Quantum Electron.*, vol. 20, no. 6, p. 3803507, Nov./Dec. 2014.

[24] J.-M. Wun, H.-Y. Liu, Y.-L. Zeng, C.-B. Huang, C.-L. Pan, and J.-W. Shi, "High-power THz-wave generation by using ultra-fast (315 GHz) uni-traveling carrier photodiode with novel collector design and photonic femtosecond pulse generator," presented at the Optical Fiber Communications Conference. and Exhibition , Los Angeles, CA, USA, Mar. 2015, Paper M3C.6.

[25] M. Levinshtein, S. Rumyantsev, and M. Shur, *Handbook Series on Semiconductor Parameters*. Singapore: World Scientific, 1996.

[26] Y.-S. Wu, J.-W. Shi, and P.-H. Chiu, "Analytical modeling of a high-performance near-ballistic uni-traveling-carrier photodiode at a 1.55 μm wavelength," *IEEE Photon. Technol. Lett.*, vol. 18, no. 8, pp. 938–940, Apr. 2006.

[27] T. Ishibashi, "Nonequilibrium electron transport in HBTs," *IEEE Trans. Electron Devices*, vol. 48, no. 11, pp. 2595–2604, Nov. 2001.

[28] A. Hirata, T. Furuta, H. Ito, and T. Nagatsuma, "10-Gb/s millimeter-wave signal generation using photodiode bias modulation," *J. Lightw. Technol.*, vol. 24, no.4, pp. 1725–1731, Apr. 2006.

[29] M. Chtioui, F. Lelarge, A. Enard, F. Pommereau, D. Carpentier, A. Marceaux, F. V. Dijk, and M. Achouche, "High responsivity and high power UTC and MUTC GaInAs-InP photodiodes," *IEEE Photon. Technol. Lett.*, vol. 24, no. 4, pp. 318–320, Feb. 2012.

[30] A. Hirata, M. Harada, and T. Nagatsuma, "120-GHz wireless link using photonic techniques for generation, modulation, and emission of millimeter-wave signals," *J. Lightw. Technol*., vol. 21, no. 10, pp. 2145–2157, Oct. 2003.

[31] C.-B. Huang and Y. Lai, "Loss-less pulse intensity repetition-rate multiplication using optical all-pass filtering," *IEEE Photon. Technol. Lett.*, vol. 12, no. 2, pp. 167–169, Feb. 2000.

[32] F.-M. Kuo, C.-B. Huang, J.-W. Shi, N.-W. Chen, H.-P. Chuang, J. E. Bowers, and C.-L. Pan, "Remotely up-converted 20 Gbit/s error-free wireless on-off-keying data transmission at W-band using an ultra-wideband pho-

tonic transmitter-mixer," *IEEE Photon. J.*, vol. 3, no. 2, pp. 209–219, Apr. 2011.

[33] N.-W. Chen, J.-W. Shi, F.-M. Kuo, J. Hesler, T. W. Crowe, and J. E. Bowers, "25 Gbits/sec error-free wireless link between ultra-fast W-band photonic transmitter-mixer and envelop detector," *Opt. Exp.*, vol. 20, no. 19, pp. 21223–21234, Sep. 2012.

Jhih-Min Wun was born in Taoyuan, Taiwan, on October 03, 1988. He is currently working toward the Ph.D. degree at the Department of Electrical Engineering, National Central University, Taoyuan, Taiwan. His current research interests include high-speed optoelectronic device measurement and sub-THz high-speed photodiode.

Hao-Yun Liu was born in Hualien City, Taiwan, on November, 18, 1991. He recieved the B.S. degree from the Department of Electrical Engineering, National Tsing-Hua University, Hsinchu, Taiwan. He is currently working toward the M.S. degree in the Institute of Photonics Technologies, National Tsing-Hua University. His current research interests include high repetition rate pulse laser generation.

Yu-Lun Zeng, biography not available at the time of publication.

Shang-Da Yang (S'01–M'05) was born in Chiayi, Taiwan, in 1975. He received the B.S. degree in electrical engineering from National Tsing-Hua University, Hsinchu, Taiwan, in 1997, the M.S. degree in electro-optical engineering from National Taiwan University, Taipei, Taiwan, in 1999, and the Ph.D. degree from the School of Electrical and Computer Engineering, Purdue University, West Lafayette, IN, USA, in 2005, respectively. He was an Assistant Professor at National Tsing-Hua University in 2005, and became an Associate Professor in 2010, He received the RiTEK Young Investigator Medal of the Optical Engineering Society of the republic of China in 2007. He was a Visiting Professor in Joint Institute for Laboratory Astrophysics, University of Colorado at Boulder in 2011. His research interests include ultrasensitive femtosecond pulse measurements, characterizations of optical frequency combs, quasi-phase matching engineering, and femtosecond fiber oscillators.

Ci-Ling Pan (M'88–SM'03–F'12) is a Tsing Hua Chair Professor and a Chairperson of the Department of Physics and Institute of Astronomy, National Tsing Hua University (NTHU), Hsinchu, Taiwan. He held joint appointment with the Institute of Photonics Technologies and served as the Director of the Photonics Research Center of NTHU. He was with National Chiao-Tung University, Hsinchu, from 1981 to 2009. He was a Visiting Professors at Osaka University, Osaka, Japan, and Chinese University of Hong Kong, Hong Kong, in 2004 and 2008, respectively. His research focuses on ultrafast and THz photonics. His current research interests include the developments of functional liquid crystal THz photonic devices, femtosecond-laser re-crystallization and activation of silicon as well as novel THz generators and detectors. The latter have been used in diverse applications, such as diagnostics of technologically important materials for photovoltaics, assessing burn trauma and optical network-compatible W-band (100 GHz or 0.1 THz) wireless communication Link at a data rate beyond 20 Gb/s. He is a Fellow of APS, OSA, and SPIE.

Chen-Bin Huang (M'99–S'04–M'08) received the B.S. degree in electrical engineering from National Tsing Hua University, Hsinchu, Taiwan, in 1997, the M.S. degree in electro-optical engineering from National Chiao Tung University, Hsinchu, Taiwan, in 1999, and the Ph.D. degree from the School of Electrical and Computer Engineering at Purdue University, West Lafayette, IN, USA, in 2008. He has worked at Bell Laboratories (Alcatel-Lucent) in the USA and the Opto-Electronics & Systems (OES) Laboratories of the Industrial Technology Research Institute (ITRI) in Taiwan. He has worked as a Visiting Scientist at the Physics Institute, University of Würzburg, Germany, and the Materials Research Institute, Northwestern University, IL, USA. He joined the Institute of Photonics Technologies, National Tsing-Hua University in Taiwan as an Assistant Professor in 2008 and became an Associate Professor in 2012. His current research interests include optical and millimeter-wave arbitrary waveform generations, nanoplasmonics and applications of optical frequency combs. He has authored/co-authored one book chapter and more than 100 journal and conference papers. He is the holder of 7 U.S. patents and 13 Taiwan patents.

Prof. Huang is a Member of Photonics Society and Optical Society of America. He has served as a Regular Reviewer for *Optics Letters*, *Optics Express*, IEEE JOURNAL OF SELECTED TOPICS IN QUANTUM ELECTRONICS, IEEE PHOTONICS JOURNAL, IEEE PHOTONICS TECHNOLOGY LETTERS, IEEE TRANSACTIONS ON MICROWAVE THEORY AND TECHNIQUES, *Journal of Lightwave Technology*, *Optics Communications*, and *Applied Optics*. He received the Junior Faculty Research Award by the National Tsing Hua University, the Master's Thesis of the Year by the Optical Engineering Society of Republic of China in 1999, the Personal Research Achievement Award by OES, and the Personal Distinguished Research Achievement Award by ITRI, both in 2002. He received the Andrews and Mary I. Williams Fellowship at Purdue University, in 2004 and 2005. He was a Finalist for the IEEE/LEOS 2007 Best Student Paper Award.

Jin-Wei Shi (M'03–SM'12) was born in Kaohsiung, Taiwan, on January 22, 1976. He received the B.S. degree from the Department of Electrical Engineering, National Taiwan University, Taipei, Taiwan in 1998 and the Ph.D. degree from Graduate Institute of Electro-Optical Engineering,National Taiwan University, Taipei, Taiwan in 2002. During 2000–2001, he was a Visiting Scholar at the University of California, Santa Barbara (UCSB), CA, USA. He was a Postdoctoral Researcher at Electronic Research & Service Organization, Industrial Technology Research Institute, in 2002–2003. He joined the Department of Electrical Engineering, National Central University, Taoyuan, Taiwan, where he is currently a Professor. In 2011–2013, he joined the ECE Department of UCSB again as a Visiting Scholar. His current research interests include ultra-high speed/power optoelectronic devices, such as photodetectors, electro-absorption modulator, sub-millimeter wave photonic transmitter, and semiconductor laser. He has authored or co-authored more than 4 book chapters, 110 Journal papers, 180 conference papers, and hold 30 patents. He was the Invited Speaker of 2002 IEEE LEOS, 2005 SPIE Optics East, 2007 Asia-Pacific Microwave Photonic Conference), 2008 Asia Optical Fiber Communication & Optoelectronic Exposition & Conference, 2012 Optical Fiber Communication (OFC), 2012 Plastic Optical Fiber, and 2012 IEEE Photonic Conference. He served as the technical program committee of OFC 2009–2011, 2012 SSDM, 2012 MWP, 2013 Asia-Pacific CLEO, and 2014 IPRM. He received the year 2007 Excellence Young Researcher Award from Association of Chinese IEEE and the 2010 Da-You Wu Memorial Award.